Assessing the effect of magnetite nanoflowers on platelets in a multiscale approach in the context of thromboembolic diseases

Monika Colombo, Yingchao Meng, Marie Poirier-Quinot, Anne-Laure Rollet, Audrey Geeverding, Mihaela Delcea, Andrew Demello, Ali Abou-Hassan

Assessing the Effect of Magnetite Nanoflowers on Platelets in a Multi-scale Approach in the Context of Thromboembolic Disease

Monika Colombo*[A,B,‡], Yingchao Meng[B], Marie Poirier-Quinot[C], Anne-Laure Rollet[D], Audrey Geeverding[E], Mihaela Delcea[F], Andrew J deMello[B], and Ali Abou-Hassan*[,D,G,‡]

[A.] Monika Colombo
Department of Mechanical and Production Engineering, Aarhus University, Aarhus, Denmark
[B.] Monika Colombo, Yingchao Meng, Andrew J deMello
Department of Chemistry and Applied Biosciences, Institute for Chemical and Bioengineering, ETH Zürich, Zürich, Switzerland.
[C]. Marie Poirier-Quinot
Université Paris-Saclay, CNRS, Inserm, Laboratoire d'Imagerie Biomédicale Multimodale Paris Saclay, Orsay, France
[D]. Ali Abou-Hassan, Anne-Laure Rollet
Sorbonne Université, CNRS, PHysico-chimie des Electrolytes et Nanosystèmes InterfaciauX, PHENIX, F-75005 Paris, France.
[E.] Audrey Geeverding
Sorbonne Université, CNRS, Institut de Biologie Paris-Seine (IBPS), Service de microscopie électronique (IBPS-SME), F-75005, Paris
[F.] Mihaela Delcea
Department of Biophysical Chemistry, Institute of Biochemistry, University of Greifswald 17487 Greifswald, Germany
[G.] Ali Abou-Hassan
Institut Universitaire de France (IUF), 75231 Paris Cedex 05, France

Keywords: Magnetite nanoflowers, blood, nano-bio interactions, platelet activation, vascular diseases

Abstract: Iron oxide magnetic nanoparticles have emerged as promising theranostic agents for cardiovascular diseases. Using a multiscale approach, we investigated the interaction of 26.5 nm diameter multicore magnetite nanoflowers, recognized for being excellent nanoheaters and contrast agents in nanomedicine, with human blood platelets. Using flow cytometry, we determined safe concentration levels of magnetite nanoflowers. Data indicated that platelets exhibit reversible activation at high magnetite nanoflowers concentrations. Magnetic resonance imaging revealed significant reductions in T1 and T2 relaxation times when platelets were combined with magnetite nanoflowers at high concentrations suggesting nanoparticle - platelets interaction. At the nanoscale, transmission and scanning electron microscopy confirmed morphological changes in platelets when exposed to high concentration of nanoparticles and their partial internalization in the platelets. Overall, the findings support the theranostic potential of magnetite nanoflowers in whole blood for thromboembolic disease management, with potential for future investigations over longer exposure.

1. Introduction

Iron oxide magnetic nanoparticles (NPs) have gained significant attention as theranostic agents in a range of biomedical applications, including the treatment of cardiovascular diseases.[1–5] The versatility of magnetic NPs enables precise magnetic manipulation, drug delivery, imaging, and therapeutic interventions at both cellular and molecular level, addressing the complex challenges posed by cardiovascular disorders.[3,6–8] Given their biocompatibility and magnetic properties,[9] these NPs are primarily employed as thermal therapies for magnetic hyperthermia and as contrast agents in magnetic resonance imaging (MRI) even in microvasculature, enhancing diagnostic capabilities.[2,10–15] Furthermore, the utilization of magnetic iron oxides in photothermal therapy has gained popularity, particularly in the context of obstructive diseases associated with blood clotting and thromboembolic events.[16] As demonstrated in cancer therapy, multicore iron oxide nanoflowers (IONFs) are able to convert absorbed near-infrared light into heat and, thus, to act as heat mediators in targeted photothermal therapy.[17–23]

Besides traditional application in cancer treatment, magnetic NPs have recently been used to treat local and systemic vascular diseases, such as atherosclerosis and thrombosis.[2] They can be used in hyperthermal vascular treatment to improve blood flow.[24] The potential use of IONPs for the treatment of diseases, such as thrombosis, is especially attractive when addressing regions of the microcirculation that cannot be reached using established approaches. Here, the use of nanotheranostics improves both the imaging and the treatment delivery.[25]

One of the primary concerns when using NPs is their potential toxicity, which will vary depending on both nanoparticle's structure (e.g. shape, size, crystallinity, phase purity, surface chemistry), polydispersity and dose.[26,27] While iron oxide NPs are generally considered to be biocompatible, excessive accumulation or prolonged exposure may lead to adverse effects, necessitating careful evaluation of their safety profiles.[28] Moreover, the susceptibility of these NPs to *in vivo* modifications (i.e. aggregation and degradation) can affect their magnetic properties and their theranostic efficacy, making it crucial to develop stable formulations for consistent performance.[29] For example, the hemolytic response of iron oxide has previously been assessed by exposing human red blood cells to iron oxide magnetic NPs. Such investigations have confirmed morphological changes that vary as a function of the NP concentration.[30] Moreover, loading efficiencies will depend on the nature of the targeted cells, as demonstrated by previous research with iron oxide NPs in both cancer therapies [18,31] and vascular thromboembolic disease management.[32,33]

Herein, we present a multiscale physico-chemical approach to assess the interaction of IONFs with human blood platelets (PLT). Specifically, we use flow cytometry and MRI to study primary cytocompatibility and relaxation properties, to probe the interaction of IONFs with the biological human blood environment. Additionally, transmission (TEM) and scanning electron microscopy (SEM) are used to investigate localization of IONFs at the nanoscale. IONFs were chosen due to their multimodality as theranostics. Indeed, they are known to be amongst the best nanoheaters used in magnetic hyperthermia and photothermia,[18] in addition to being excellent T2 contrast agents.[20] In a theranostic context, these modalities are ideal for future applications in imaging and treating of cardiovascular diseases. Our investigations as represented in Figure 1 assess the interaction of IONFs with PLT isolated from fresh human blood. The safe interaction between IONFs and human blood represents the first step of their action as nanomedicine for obstructive and thromboembolic diseases.

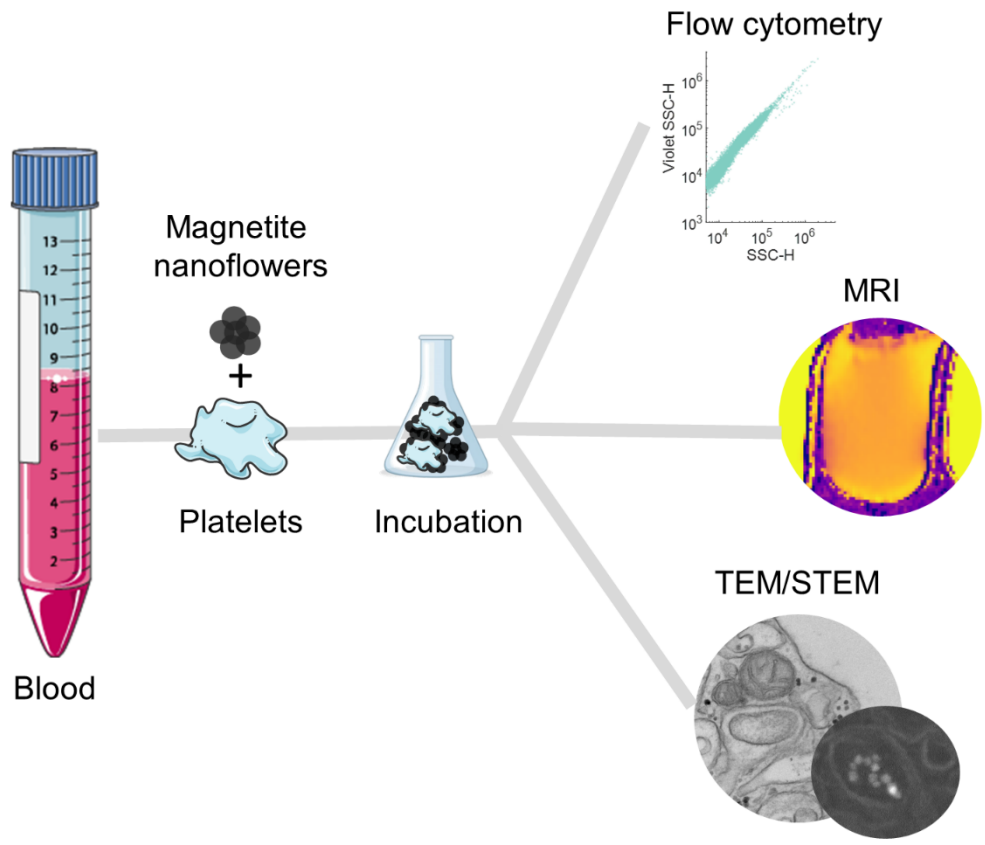

Fig. 1 – Graphical workflow showing the multi-scale approach used to study the interaction of iron oxide magnetic nanoparticles with human blood cells for future application to thromboembolic diseases. MRI: Magnetic resonance imaging; TEM: Transmission electron microscopy; STEM: Scanning transmission electron microscopy

2. Experimental section

2.1 Preparation of IONFs

All the reagents used were of analytical purity and used as received. NPs were prepared according to a protocol developed in our previous work.[18] Ethyl acetate (>99.5%), acetone (technical grade), ethanol (96%), diethyl ether (100%), N-methyldiethanolamine (NMDEA, 99%), and diethylene glycol (DEG, 99%) were obtained from Sigma-Aldrich (Saint Quentin Fallavier, France). Sodium hydroxide (NaOH, 98%), iron(III) nitrate nonahydrate ($Fe(NO_3)_3$•$9H_2O$, >98%), and iron(II) chloride tetrahydrate ($FeCl_2$•$4H_2O$, 98%) were from Alfa Aesar (Haverhill, MA, USA). Iron(III) chloride hexahydrate ($FeCl_3$•$6H_2O$, >97%) was obtained from Panreac Quimica SLU (Castellar del Valles, Spain). The polyol process was used to prepare magnetite Fe_3O_4 nanoflowers in polyol solvents at 220°C.[20–23] After synthesis, IONFs were flocculated, washed and resuspended in water. To prevent IONF aggregation in physiological buffers, nanoflowers were coated with citrate. Citrate and the iron oxides were mixed in a molar ratio mol Fe/mol citrate = 0.13, and kept at 80°C for 30 minutes to promote adsorption of citrate anions onto nanoparticle surfaces.[18,34]

2.2 Dynamic light scattering (DLS) measurements

IONF hydrodynamic diameters were measured using a Zetasizer Nano ZS system (Malvern Instruments, Malvern, UK) operating at 20 °C in backscatter mode at optical configuration of 173°.

2.3 Fresh human blood samples

Blood samples from healthy donors were obtained from the blood donation center *Blutspende Zürich* (Schlieren, Switzerland). The study was conducted in accordance with the principles of the Declaration of Helsinki, and the project was approved by the Swiss Association of Research Ethics Committees (BASEC-Nr: 2019-01721). Fresh samples were shipped in dry ice and kept at 4°C for a maximum of 48 hours. Standard protocols for the fractionation of human whole blood were followed. A commercial density-gradient medium (Lymphoprep™, STEMCELL Technologies, Vancouver, Canada) was used to isolate mononuclear cells. After adding it to whole blood, the solution was centrifuged at 800 g for 30 minutes. The obtained sample comprised a bottom layer of red blood cells, a buffy coat consisting of suspended white blood cells and PLT, and a top layer of plasma, proteins, and PLT. The efficacy of fractionation

protocol was verified by flow cytometry (Figure S1). The individual components (from top to bottom layer) were gently moved into Eppendorf cuvettes or falcon tubes according to the desired quantities for analysis.

2.4 Platelet viability protocol

PLT were obtained after blood fractionation, yielding a PLT-rich plasma solution. To prevent mechanical activation of PLT, further centrifugation and washing was avoided.[35] Initial verification of PLT viability was performed using a CytoFLEX flow cytometer (Beckman Coulter, Pasadena, USA). To avoid overflow, PLT-rich plasma was diluted by transferring 5 µL of solution in 295 µL of phosphate-buffered saline (PBS) in a 96-well for flow cytometry analysis. Forward and side scatter were used to correlate signal with cell size. The final solution was prepared by mixing PLT-rich plasma in PBS at a ratio 1:3, namely 250 µL in 750 µL of PBS. Using gentle mixing to avoid activation, a homogeneous solution of PLT-rich plasma and PBS was considered for the treatment (control, distilled water, and IONFs concentrations). The treatment was added in a ratio of 1:10 of the PBS component into an Eppendorf cuvette. Following incubation of 30 minutes, 3 hours or 6 hours at room temperature, solutions were analyzed by flow cytometry as described above. Standard gating for human blood samples was followed.[36]

2.5 MRI experiments

Plasma was separated from fresh human blood sample as described in 2.3. PLT-rich plasma in PBS (ratio 1:3, as previously described in 2.4) was mixed gently with a certain volume of IONFs to reach a final concentration (C_1 and C_3). Further centrifugation was avoided to limit the PLT pre-clinical activation.[35] Experiments were performed in the BioMaps Laboratory at the University of Paris-Saclay (France). MRI experiments were performed at 3.0 T (^{1}H Larmor frequency of 128 MHz) on a USA Signa^{TM} PET/MRI scanner (GE Healthcare Technologies Inc, Chicago, USA). Two rounds of experiments (T1 and T2 mapping) were performed at 5, 30, 45 and 65 minutes after an incubation period of 30 minutes for the IONFs-C_1 and IONFs-C_3 samples.[37] T1 mapping was performed using an inversion recovery sequence with 6 values of inversion recovery time (50, 200, 300, 600, 1000 and 1977 ms), an echo time of 11 ms, a repetition time of 2000 and an acquisition time of 3 minutes. T2 mapping followed a GE dedicated sequence, with 16 echo times varying between 8.9 and 142 msec, a repetition time of 1200 and an acquisition time of 3.15 minutes. T1 and T2 values were measured at three regions

of interest (ROIs) located at the top, middle and bottom of the sample. This was done to account for the effect of gravity and sedimentation on the blood sample.

2.6 Fast field cycling nuclear magnetic resonance spectroscopy (NMR) relaxation

The measurements of the water 1H longitudinal relaxation rates $R_1 = \frac{1}{T_1}$ have been performed Stelar SpinMaster NMR relaxometer (Mede, Italy) in the frequency range 10 kHz to 30 MHz (1H frequency). T1 has been measured using a pre-polarized sequence from 10 kHz to 10 MHz and a non-polarized sequence from 10 MHz to 30 MHz.[38] The recycle delay was set at 10 times T1 and the magnetization curve spanned from 0.01 T1 to 4 T1.

2.7 Transmission electron microscopy

After 30-minute incubation of PLT with IONFs as described for MRI experiments, the mixture was slowly centrifuged (800 g, 5 minutes) to form a pellet and avoid activation of PLT. The effect of centrifugation was assessed on PLT without IONFs (control). The supernatant was removed, and the pellets were fixed with 1.5 % glutaraldehyde and 1 % PFA in 0.1 M cacodylate buffer (pH 7.4) overnight at 4°C. Further steps were assisted with a Pelco Biowave Pro+ (Ted Pella Inc., Redding, CA, USA) microwave device: 3 buffer washes with cacodylate buffer 0.1 M (200 W 40 s), 0.2 % OTE in 0.1 M cacodylate buffer (150 W ON/OFF/ON cycles 7 x 2 min), 3 buffer washes with cacodylate buffer 0.1 M (200 W 40 s), 1 % osmium tetroxide in 0.1 M cacodylate buffer (100 W ON/OFF/ON cycles 7 x 2 min) and 3 deionized water washes (200 W 40 s). PLT were pre-embedded with 4 % agarose in deionized water, dehydrated through a graded concentration of ethanol 50-70-95-100-100 % then acetone 100-100 % (200 W 40 s), infiltrated with a graded concentration of acetone and Epon resin mix 10-25-50-75-90 % and 3 times with 100 % Epon resin (200 W 5 min). Resin infiltration steps were performed under vacuum (20 mm Hg). Samples were embedded in silicone mold with resin and polymerized at 60° C for 72 hours. 70 nm ultrathin sections were cut with an Ultracut ultramicrotome (UCT, Leica microsystems, Wetzlar, Germany) deposited on 150 mesh copper grids, and contrasted with 2.5 % uranyl acetate and 2 % lead citrate. Observations were performed using a LaB6 JEM 2100 HC TEM (Jeol, Basiglio, Italy) at 80 kV. Acquisitions were made with a side mounted Veleta CCD camera driven by iTEM software version 5.2 (Olympus, Tokyo, Japan). Images were recorded with a 2k x 2k pixels definition (binning 1x1) and a 750 ms exposure time.

2.8 Scanning transmission electron microscopy (STEM)

For STEM-in-SEM, stained grids were first coated with 2 nm carbon using an ACE600 apparatus (Leica microsystems), before being imaged in STEM imaging mode within a field-emission scanning electron microscope (FE-SEM) GeminiSEM 500 (Carl Zeiss Microscopy, Oberkochen, Germany) operated at 29 kV with a 15 μm aperture. Acquisitions were done in both bright-field and High Angle Annular Dark-Field imaging modes working in parallel (IBPS EM Facility, Sorbonne University, Paris, France).

2.9 Statistical analysis

The biological assays were triplicated for two individual donors. The relaxation times were measured independently in three different sample regions. Data are shown as means ± standard deviation, following a normality test. Statistical significance was accepted for p-values < 0.01. Given the normal distribution of the data, parametric paired t-test and ANOVA tests were conducted. All analyses were performed in MATLAB (MathWorks, Natick, MA, USA) and Origin (OriginLab Corporation, Northampton, MA, USA). Flow cytometry data were analyzed using FlowJo software (FlowJo LLC, Ashlan, OR, USA).

3. Results and Discussion

3.1 IONFs characterization

Figure 2-A shows a representative TEM image of the synthesized IONFs, and the inset showcasing their multicore nanoflower morphology. The IONFs have an average diameter, d_0, of 26.5 ± 0.6 nm and a polydispersity, σ, of 0.1 ± 0.02, as deduced from the size histogram fitted to a log-normal model (Figure 2-B). Next, the IONF concentration range was assessed, based on prior literature and clinical utility. Studies by Andreas et al. found low toxicity for nanoparticle concentrations below 100 μg Fe/mL.[39] Accordingly, we defined the treatment conditions reported in Figure 2-C. DLS measurements (Figure S2) of all IONF suspensions in PBS, showed a bimodal size distribution. A main peak located around 49 nm for all concentrations, in agreement with previous reports,[20,23] and accounting for 80% of the total intensity. Another peak with a size around 300 nm (accounting for 20%) corresponding to aggregated IONFs were also observed in C_2 and C_3 which a larger size in C_4. However as scattering intensity is proportional to the 6th power of the particle radius, the number of aggregates may be considered negligible.

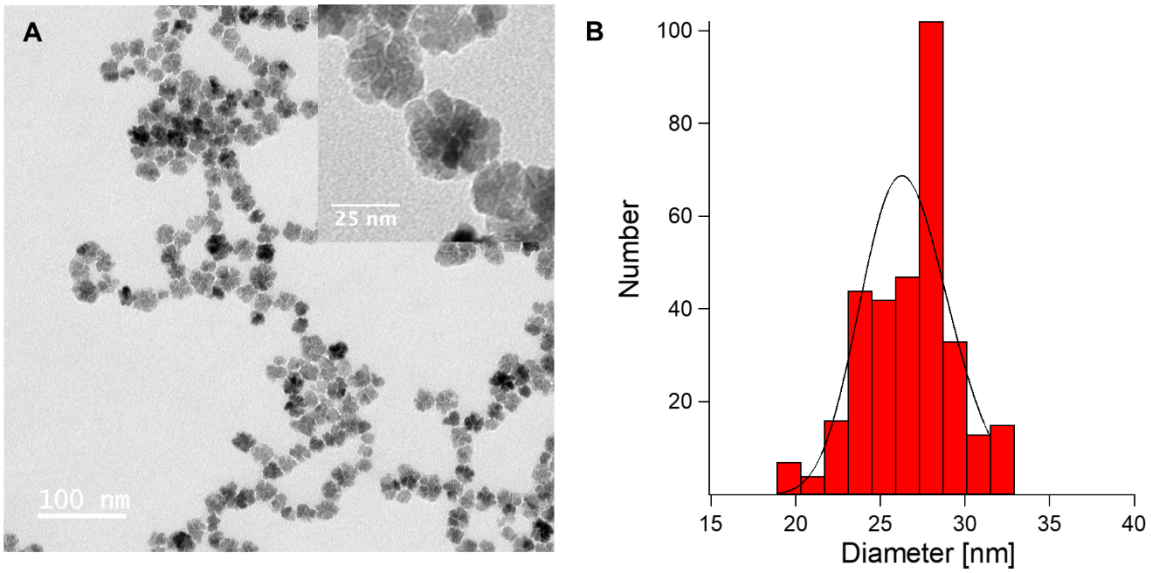

C Sample	Molar concentration (μM)	Mass concentration (μg Fe/mL)
control	0	0
C_1	1.79×10^3	100
C_2	179.0	10
C_3	17.9	1
C_4	1.79	0.1

Fig. 2 - A) Transmission electron microscopy image of magnetic IONFs used in this study; the inset shows the multicore structure of the IONFs; B) Size distribution histogram of IONFs (N=320) fitted to a Log-Normal law with $d_0 = 26.5 \pm 0.6$ and a polydispersity, σ, of 0.1 ± 0.02; C) Molar and mass concentrations of all IONFs suspensions prepared in PBS investigated in this work.

3.2 A low dose of IONFs can induce reversible PLT activation

After ensuring correct fractionation of whole blood (Figure S1), PLT viability after incubation and exposure to IONFs was assessed through flow cytometry. A control group was considered along with samples at four different IONF concentrations, and incubation times of 30 minutes, 3 hours, and 6 hours. Figure 3 presents flow cytometry violet side scatter *vs*. side scatter plots of PLT incubated for 30 minutes, where the use of violet light amplifies the difference in the refractive indices between the particles and the surrounding media. It can be seen that a sub-population (shifted to higher intensities) grows as a function of IONF concentration. This sub-population is also seen to diminish as a function of incubation times (Figure S3). Analysis of a

IONFs-C_1 solution smear under light microscopy (Figure 3-B), confirmed that PLT tend to spread as pseudopods that can extend over several micrometers from the PLT.[40] As expected, analysis of the control solution indicated no pseudopod formation. For this reason, and in agreement with previous studies on PLT, the side formation in the scatter plots was associated with morphologically changed PLT (i.e. activation induced by IONFs).

We next compared the frequency gating of the forward scatter data of the PLT baseline control condition (t_0) with the PLT incubated with IONFs-C_1 for 30 minutes, 3 hours and 6 hours (Figure 3-C and Figure S4). The frequency measurements allowed to show the percentage of cells of interest in relation to the total number of cells.[41] It is notable that in case of 30-minute incubation the trend of the frequency ratios, gated on the histogram plots of forward scattering, is opposite to that of baseline condition. Specifically, the fr_2 frequency gate is smaller than the fr_3 frequency gate for 30-minutes incubation, whereas fr_2 is larger than fr_3 for the baseline condition. However, for longer incubation times, the frequency trend is similar to that of the baseline, suggesting that PLT activation is limited in time and that exposure to IONFs-C_1 does not induce PLT apoptosis.

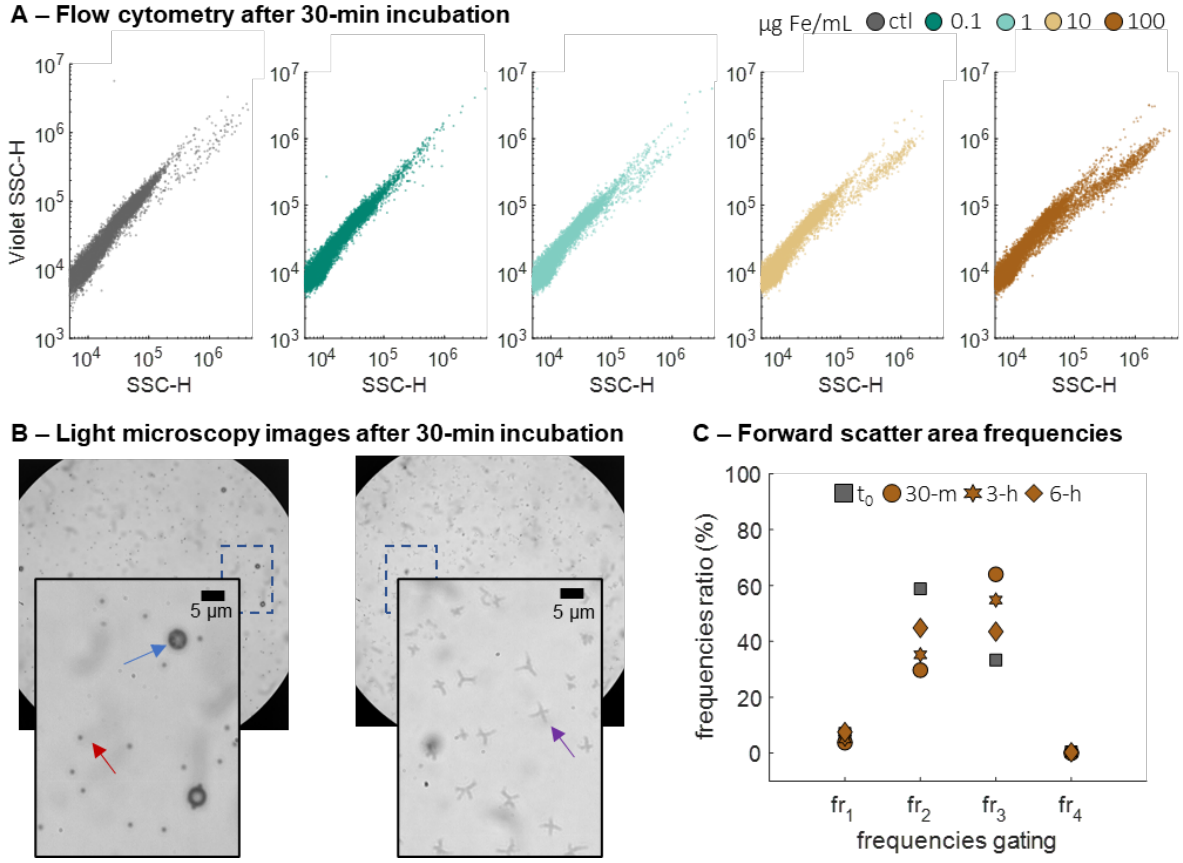

Fig. 3 – Biological characterization of IONFs after 30-minutes incubation with isolated platelets (PLT) suspended in plasma. A) Side scatter (SSC) flow cytometry plots. B) Brightfield microscopy images of a plasma smear sample after a 30-minute incubation of the control and C_1 treatment. The round black dots in (B) are identified as viable,

non-activated PLT (red arrow). Reference 5-µm polystyrene beads are also shown (blue arrow). Structures resembling PTLs pseudopods are indicated by the purple arrow. C) Comparison of the event frequencies of the forward scatter data of the PLT baseline untreated condition (t_0, grey square) and PLT incubated with IONFs-C_1 for 30 minutes (brown circle), 3 hours (brown hexagram), and 6 hours (brown diamond).

3.3 Interaction of IONFs with PLT at high concentration induces changes in MRI relaxivity

Since the MRI contrast (and relaxation times) effect produced by IONFs depends on multiple parameters, including the local environment, relaxation times can be used to report nanoscale local effects. To quantify such changes, we measured at 5, 30, 45, and 65 minutes the longitudinal (T1) and transverse (T2) relaxation times, once IONFs are incubated with PLT (Figure 4).[42] Previous results have established the excellent function of IONFs as negative MRI contrast agents (T2-agents) showing an r_2 relaxivity of about 656.8 mM^{-1} s^{-1} in water and a r_1 relaxivity of approximately 10.16 mM^{-1} s^{-1} at 3T.[20]

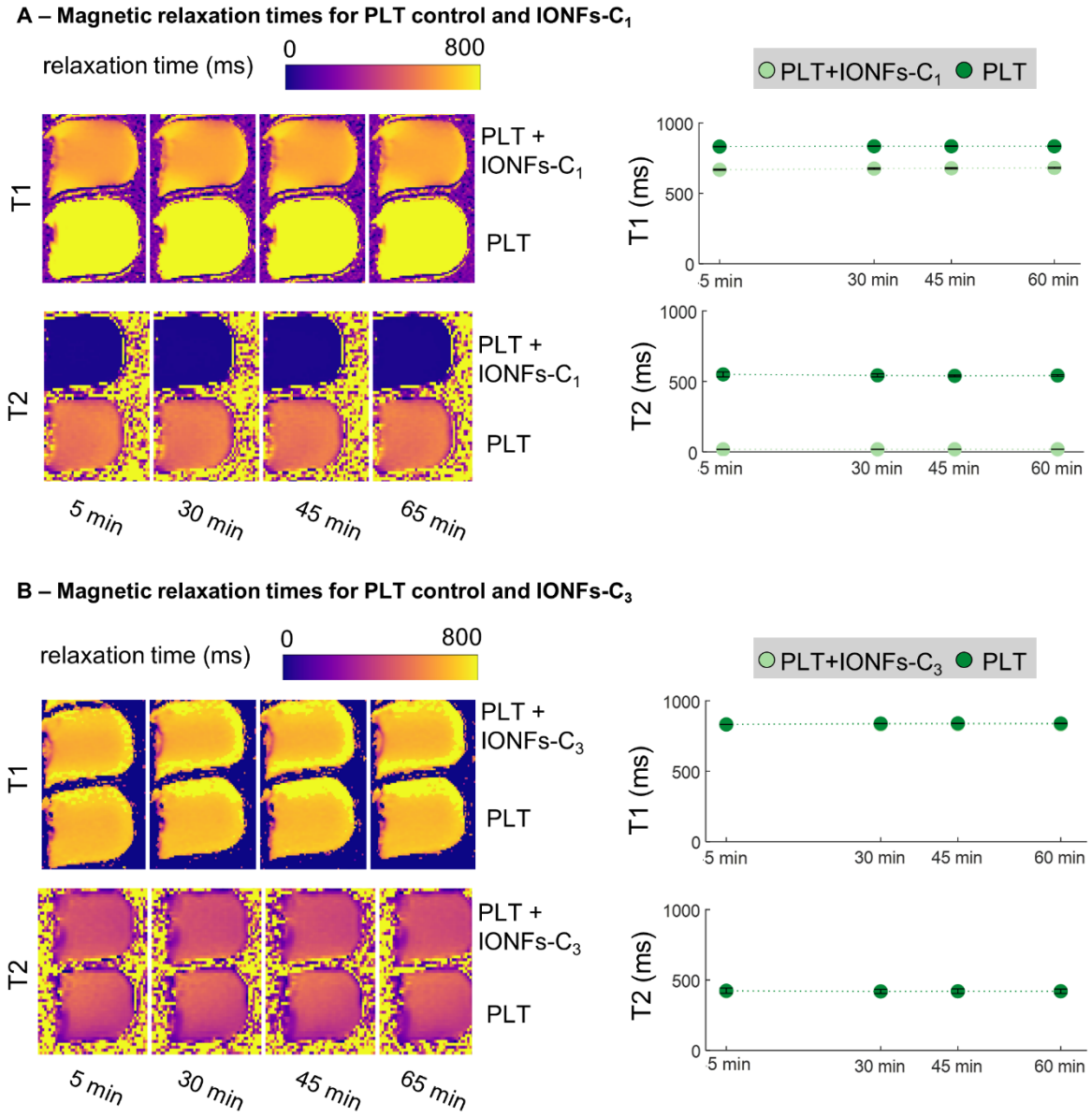

Fig. 4 – Magnetic relaxation times after 30-minute incubation of IONFs with PLT. A) on the left, T1 and T2 relaxation maps for PLT control and incubated for 30 minutes with IONFs-C_1; on the right, quantitative comparison of the T1 and T2 measurements across 3 regions of interest (ROIs) for each time point (5, 30, 45 and 65 minutes) for control and IONFs-C_1 solutions. B) on the left, T1 and T2 relaxation maps for PLT control and incubated for 30 minutes with IONFs-C_3; on the right, quantitative comparison of the T1 and T2 measurements across 3 ROIs for each time point (5, 30, 45 and 65 minutes) for control and IONFs-C_3 solutions.

After incubating the IONFs with PLT (for IONFs-C_1 and IONFs-C_3), MRI images were acquired at different times to extract T1 and T2 relaxation times. Figure 4-A presents the relaxation maps for PLT controls and IONFs-C_1 treated solutions, while Figure 4-B shows the dual maps of PLT treated with IONFs-C_3. For both concentrations, relaxation times of all the solutions were relatively constant over the considered time span. We then quantified the T1 and T2 relaxation times in three different ROIs in the sample, considering the effects of gravity on

PLT sedimentation over time. For example, for 30 minutes, in the same ROI, the addition of the IONFs to PLT induced a decrease in T1 and T2 relaxation times. Indeed, T1 relaxation times of the solutions of PLT (676 ± 6 ms) with IONFs-C1 (Figure 4-A and Table S1) were statistically different from control PLT (834 ± 2 ms), with p-values of 0.00034.

In the case of IONFs-C_3, no statistical difference was observed for the T1 relaxation time when added to PLT (with p-values of 0.04). Namely, the T1 relaxation time for PLT (832 ± 3 ms) with IONFs-C_3 was comparable to the PLT control (839 ± 1 ms). When considering the T2 relaxation times (Table S3-4), data indicate a more significant impact. Indeed, values for PLT (19 ± 1 ms) incubated for 30 minutes with IONFs-C_1 were statistically different to the control PLT (543 ± 13 ms), with p-values of 0.00021, respectively (Figure 4-B, Table S3). Conversely, for the lower concentration IONFs-C_3, no statistical differences in T2 relaxation time were found for PLT (420 ± 10 ms) when compared to the control PLT (419 ± 18 ms) solutions (p-value of 0.87).

To better understand these observations, fast field cycling NMR relaxometry, that gives access to the surface accessible to water molecules was recorded. NMR relaxation profiles were recorded for the same samples and after 30-minute incubation time of PLT with IONFS-C_1 or C_3 solutions. The results show that the concentration C_3 in IONFs is not sufficient to induce an enhancement of the NMR relaxation that is masked by the experimental uncertainties (Figure S5). Consequently, the NMR relaxation profiles of IONFs-C_3 and PLT are similar and close to 0.5 s^{-1}, i.e., the R_1 of the bulk alone. On the contrary, C_1 concentration is high enough to induce an important increase of R_1. Two results can be underlined from Figure S6. First, the shape of the NMR relaxation profiles is very close to each other, meaning that there is no modification of the magnetic properties of the IONFs, as aggregation could do alone. Second, the R_1 values follow the following order water>PLT>PBS, that may be attributed to a decrease of the IONFs surface accessibility by water molecules.[43–45] Based on these observations we may hypothesize an interaction between IONFs and PLT. In addition, despite the low concentration of C_1, IONFs can still induce a significant reduction in both longitudinal T1 and transverse T2, confirming their function as effective MRI contrast agents.

3.4 IONFs can be internalized in PLT at high concentration

To assess the localization of IONFs at the nanoscale and the morphological changes that they may induce once in contact with PLT, we acquired TEM and STEM images of PLT exposed to IONFs-C_1 and IONFs-C_3 concentrations and control for 30 minutes (see experimental section), as shown in Figure 5. STEM-in-SEM in the bright and the dark field modes were used to

distinguish the IONFs from organic particles such as glycogen (Figure 5-B).[46] Compared to the bright field mode useful to image the morphology of cells and IONFs size and shape, the bright field mode allows to discriminate between species based on their electronic density. Consequently, IONFs appear brighter than glycogen which in addition to the differences in the size and shape helps to identify them easily. TEM and STEM images showed α-granules typical of PLT.[40,47] When exposed to IONFs-C_1, the shape of PLT was more elongated when compared to the control and IONFs-C_3 samples from the same blood sample and for the same incubation time.

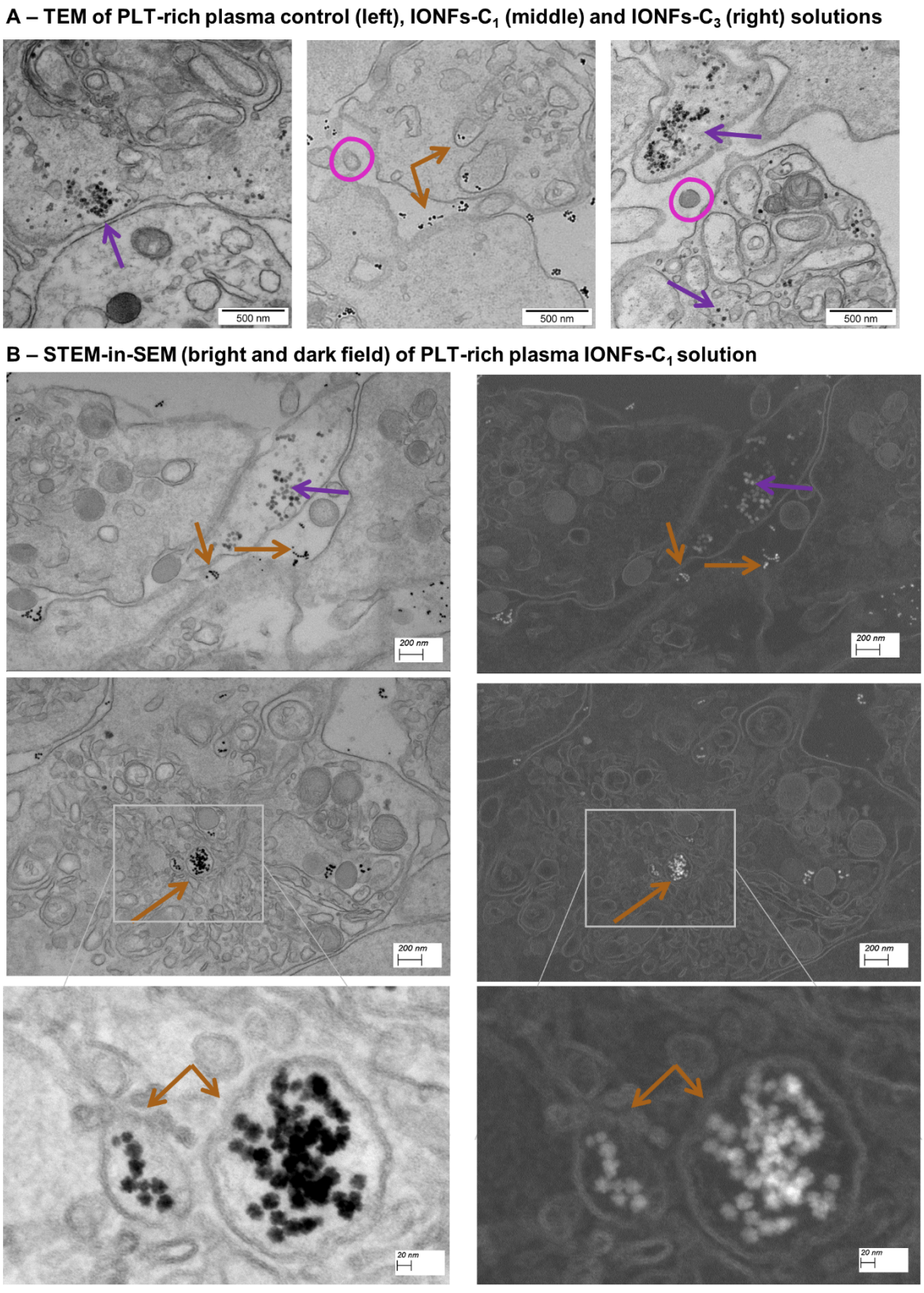

Fig. 5: A) TEM of PLT-rich plasma in the case of control; C_1 and C_3 nanoflowers concentrations, after a 30-minute incubation. B) STEM-in-SEM images in the bright-field (left) and high angle annular dark-field imaging (right) modes in the case of IONFs-C_1. Glycogen (purple arrow); IONFs (brown arrow); ectosome-like formations (pink circles). More STEM-in-SEM images are provided in Figures S8 and S9 in SI.

In agreement with previous studies, it was possible to identify in both the control and IONFs-C_3 an abundance of glycogen granules (spheroidal formations about 50 nm in size) contained within the PLT cytoplasm (see also Figure S7).[40,46] It is observed that in case of IONFs-C_1, glycogen agglomerations were less abundant or barely identifiable. Glycogen is indeed known to serve as reservoir for energy production in PLT; during PLT activation (a transition from low-energy resting states to high-demanding metabolic states) glycogen is degraded through glycogenolysis.[46,48] This suggests that the IONFs-C_1 has induced transition to a high-demanding state where the stored glycogen is engaged.[40,46] In case of IONFs-C_1, individual or aggregated IONFs were seen both in the extracellular and intracellular environment, as indicated by brown arrows. As shown from STEM images in Figure 5-B (see also Figure S8), IONFs-C_1 were randomly located in the extracellular environment, on the PLT membranes and inside the endosomes where the typical flower-shape was observed at high magnification images. On the contrary, after 30-minute incubation of PLT with IONFs-C_3, in addition of being rare, IONFs were localized mainly in the extracellular environment (Figure S9) and no internalization was observed based on STEM images. In addition, for C_3 concentration an abundance of particulate matter (50-60 nm in size) related to glycogen was found. Finally, vesicular formation referable to ectosomes could be visualized in the case of IONFs-C_1, and in lower amount, of IONFs-C_3 and control (indicated by pink circles).[49] To conclude, TEM and STEM images are in good agreement with the biological data and MRI showing that IONFs-C_1 concentration can induce notable alterations to PLT, while undergoing membrane interaction and sometimes internalization.

4. Conclusion

We have investigated the interaction of IONFs with blood components, focusing on the primary biological changes of PLT. By employing fresh human blood, we selected different IONFs concentration levels, and studied the effects on isolated PLT. From the biological standpoint, PLT were appreciably affected by incubation with the highest IONFs concentration for 30 minutes. This activation, however, disappeared after further incubation. From MRI measurements, a substantial reduction of the T1 and T2 relaxation times for IONFs-C_1 was seen when compared to the control cases in PLT populations. Lower concentrations of IONFs (IONFs-C_3) induced negligible effects compared to the control. Finally, TEM and STEM images showed that in PLT-rich plasma exposed to IONFs-C_1, PLT could partially internalize IONFs. Accordingly, we conclude that IONF concentrations close to C_1 in human blood can induce temporary morphological changes in PLT.

A key parameter that was not taken into account in our study is the residence time that nanoparticles can spend into the blood (e.g. 7 min).[50] This residence time may compromise the interaction of IONFs with PLT and their predetermined functions. As the residence time is determined by many parameters including their intrinsic physicochemical properties and the physiological environment,[51] quantifying the kinetic disposition *in vivo* of these nanoparticles will be a priority before any future medical application.

ASSOCIATED CONTENT

Supporting Information.

Flow cytometry data of the fractionated blood samples, flow cytometry of the PLT before and after exposition to IONFs, DLS measurements, TEM and STEM images of platelets incubated with different concentrations of IONFs, NMR relaxometry measurements and table of relaxation times (file type, i.e., PDF)

AUTHOR INFORMATION

Corresponding Author

Monika Colombo mc@mpe.au.dk
Ali Abou-Hassan ali.abou_hassan@sorbonne-universite.fr

Author contributions

The manuscript was written through contributions of all authors. All authors have given approval to the final version of the manuscript. ‡These authors contributed equally.

M.C: Conceptualization; Data curation; Formal analysis; Investigation; Methodology; Project administration; Writing - original draft; and Writing - review & editing.

Y.M: Investigation; Methodology; and Writing - review & editing.

M.P.-Q: Investigation; Methodology; Writing - original draft; and Writing - review & editing.

A.-L.R: Methodology, Writing - review & editing.

A.G: Investigation, Writing - review & editing.

M.D.: Writing - review & editing.

A.J.dM: Funding acquisition; Resources; Supervision; Writing - review & editing

A.A.-H: Conceptualization; Data curation; Formal analysis; Funding acquisition; Investigation; Methodology; Project administration; Resources; Supervision; Writing - original draft; and Writing - review & editing.

Acknowledgements

M.C. acknowledges support from Aarhus University and ETH Zurich. A.A.-H. acknowledges support from the Institut Universitaire de France**.** A.J.dM acknowledges support from ETH Zurich. We acknowledge Alexis Canette and Michaël Trichet from the IBPS electron microscopy core facility for their contribution and the support of « Région Île-de-France », Sorbonne-Université and CNRS.

Conflict of Interest

The authors declare no conflict of interest.

References

(1) Younis, N. K.; Ghoubaira, J. A.; Bassil, E. P.; Tantawi, H. N.; Eid, A. H. Metal-Based Nanoparticles: Promising Tools for the Management of Cardiovascular Diseases. *Nanomedicine: Nanotechnology, Biology and Medicine* **2021**, *36*, 102433. https://doi.org/10.1016/j.nano.2021.102433.

(2) Vazquez-Prada, K. X.; Lam, J.; Kamato, D.; Xu, Z. P.; Little, P. J.; Ta, H. T. Targeted Molecular Imaging of Cardiovascular Diseases by Iron Oxide Nanoparticles. *Arteriosclerosis, Thrombosis, and Vascular Biology* **2021**, *41* (2), 601–613. https://doi.org/10.1161/ATVBAHA.120.315404.

(3) Omidian, H.; Babanejad, N.; Cubeddu, L. X. Nanosystems in Cardiovascular Medicine: Advancements, Applications, and Future Perspectives. *Pharmaceutics* **2023**, *15* (7), 1935. https://doi.org/10.3390/pharmaceutics15071935.

(4) Cazares-Cortes, E.; Wilhelm, C.; Efrain Perez, J.; Espinosa, A.; Casale, S.; Michel, A.; Abou-Hassan, A.; Ménager, C. Tuning the Load of Gold and Magnetic Nanoparticles in Nanogels through Their Design for Enhanced Dual Magneto-Photo-Thermia. *Chemical Communications* **2021**, *57* (48), 5945–5948. https://doi.org/10.1039/D0CC07176E.

(5) Cazares-Cortes, E.; Cabana, S.; Boitard, C.; Nehlig, E.; Griffete, N.; Fresnais, J.; Wilhelm, C.; Abou-Hassan, A.; Ménager, C. Recent Insights in Magnetic Hyperthermia: From the "Hot-Spot" Effect for Local Delivery to Combined Magneto-Photo-Thermia Using Magneto-Plasmonic Hybrids. *Advanced Drug Delivery Reviews* **2019**, *138*, 233–246. https://doi.org/10.1016/j.addr.2018.10.016.
(6) Serio, F.; Silvestri, N.; Kumar Avugadda, S.; Nucci, G. E. P.; Nitti, S.; Onesto, V.; Catalano, F.; D'Amone, E.; Gigli, G.; del Mercato, L. L.; Pellegrino, T. Co-Loading of Doxorubicin and Iron Oxide Nanocubes in Polycaprolactone Fibers for Combining Magneto-Thermal and Chemotherapeutic Effects on Cancer Cells. *Journal of Colloid and Interface Science* **2022**, *607*, 34–44. https://doi.org/10.1016/j.jcis.2021.08.153.
(7) Fernandes, S.; Fernandez, T.; Metze, S.; Balakrishnan, P. B.; Mai, B. T.; Conteh, J.; De Mei, C.; Turdo, A.; Di Franco, S.; Stassi, G.; Todaro, M.; Pellegrino, T. Magnetic Nanoparticle-Based Hyperthermia Mediates Drug Delivery and Impairs the Tumorigenic Capacity of Quiescent Colorectal Cancer Stem Cells. *ACS Appl. Mater. Interfaces* **2021**, *13* (14), 15959–15972. https://doi.org/10.1021/acsami.0c21349.
(8) Demri, N.; Dumas, S.; Nguyen, M.-L.; Gropplero, G.; Abou-Hassan, A.; Descroix, S.; Wilhelm, C. Remote Magnetic Microengineering and Alignment of Spheroids into 3D Cellular Fibers. *Advanced Functional Materials* **2022**, *32* (50), 2204850. https://doi.org/10.1002/adfm.202204850.
(9) Arias, L. S.; Pessan, J. P.; Vieira, A. P. M.; de Lima, T. M. T.; Delbem, A. C. B.; Monteiro, D. R. Iron Oxide Nanoparticles for Biomedical Applications: A Perspective on Synthesis, Drugs, Antimicrobial Activity, and Toxicity. *Antibiotics (Basel)* **2018**, *7* (2), 46. https://doi.org/10.3390/antibiotics7020046.
(10) Khurshid, H.; Friedman, B.; Berwin, B.; Shi, Y.; Ness, D. B.; Weaver, J. B. Blood Clot Detection Using Magnetic Nanoparticles. *AIP Adv* **2017**, *7* (5), 056723. https://doi.org/10.1063/1.4977073.
(11) Karagkiozaki, V.; Pappa, F.; Arvaniti, D.; Moumkas, A.; Konstantinou, D.; Logothetidis, S. The Melding of Nanomedicine in Thrombosis Imaging and Treatment: A Review. *Future Sci OA* **2016**, *2* (2), 2056-562. https://doi.org/10.4155/fso.16.3.
(12) Rahman, M. Magnetic Resonance Imaging and Iron-Oxide Nanoparticles in the Era of Personalized Medicine. *Nanotheranostics* **2023**, *7* (4), 424–449. https://doi.org/10.7150/ntno.86467.
(13) Abdel-Mageed, H. M.; AbuelEzz, N. Z.; Radwan, R. A.; Mohamed, S. A. Nanoparticles in Nanomedicine: A Comprehensive Updated Review on Current Status, Challenges and Emerging Opportunities. *Journal of Microencapsulation* **2021**, *38* (6), 414–436. https://doi.org/10.1080/02652048.2021.1942275.
(14) Gavilán, H.; Avugadda, S. K.; Fernández-Cabada, T.; Soni, N.; Cassani, M.; Mai, B. T.; Chantrell, R.; Pellegrino, T. Magnetic Nanoparticles and Clusters for Magnetic Hyperthermia: Optimizing Their Heat Performance and Developing Combinatorial Therapies to Tackle Cancer. *Chem. Soc. Rev.* **2021**, *50* (20), 11614–11667. https://doi.org/10.1039/D1CS00427A.
(15) Abenojar, E. C.; Wickramasinghe, S.; Bas-Concepcion, J.; Samia, A. C. S. Structural Effects on the Magnetic Hyperthermia Properties of Iron Oxide Nanoparticles. *Progress in Natural Science: Materials International* **2016**, *26* (5), 440–448. https://doi.org/10.1016/j.pnsc.2016.09.004.
(16) Pala, R.; Pattnaik, S.; Busi, S.; Nauli, S. M. Nanomaterials as Novel Cardiovascular Theranostics. *Pharmaceutics* **2021**, *13* (3), 348. https://doi.org/10.3390/pharmaceutics13030348.
(17) Zou, L.; Wang, H.; He, B.; Zeng, L.; Tan, T.; Cao, H.; He, X.; Zhang, Z.; Guo, S.; Li, Y. Current Approaches of Photothermal Therapy in Treating Cancer Metastasis with Nanotherapeutics. *Theranostics* **2016**, *6* (6), 762–772. https://doi.org/10.7150/thno.14988.

(18) Cabana, S.; Curcio, A.; Michel, A.; Wilhelm, C.; Abou-Hassan, A. Iron Oxide Mediated Photothermal Therapy in the Second Biological Window: A Comparative Study between Magnetite/Maghemite Nanospheres and Nanoflowers. *Nanomaterials* **2020**, *10* (8), 1548. https://doi.org/10.3390/nano10081548.
(19) Walle, A. V. de; Figuerola, A.; Espinosa, A.; Abou-Hassan, A.; Estrader, M.; Wilhelm, C. Emergence of Magnetic Nanoparticles in Photothermal and Ferroptotic Therapies. *Materials Horizons* **2023**, *10* (11), 4757–4775. https://doi.org/10.1039/D3MH00831B.
(20) Benassai, E.; Hortelao, A. C.; Aygun, E.; Alpman, A.; Wilhelm, C.; Saritas, E. U.; Abou-Hassan, A. High-Throughput Large Scale Microfluidic Assembly of Iron Oxide nanoflowers@PS-b-PAA Polymeric Micelles as Multimodal Nanoplatforms for Photothermia and Magnetic Imaging. *Nanoscale Adv.* **2023**, *6* (1), 126–135. https://doi.org/10.1039/D3NA00700F.
(21) Bertuit, E.; Benassai, E.; Mériguet, G.; Greneche, J.-M.; Baptiste, B.; Neveu, S.; Wilhelm, C.; Abou-Hassan, A. Structure–Property–Function Relationships of Iron Oxide Multicore Nanoflowers in Magnetic Hyperthermia and Photothermia. *ACS Nano* **2022**, *16* (1), 271–284. https://doi.org/10.1021/acsnano.1c06212.
(22) Bertuit, E.; Menguy, N.; Wilhelm, C.; Rollet, A.-L.; Abou-Hassan, A. Angular Orientation between the Cores of Iron Oxide Nanoclusters Controls Their Magneto–Optical Properties and Magnetic Heating Functions. *Commun Chem* **2022**, *5* (1), 1–10. https://doi.org/10.1038/s42004-022-00787-0.
(23) Benassai, E.; Daffé, N.; Aygun, E.; Geeverding, A.; Ulku Saritas, E.; Wilhelm, C.; Abou-Hassan, A. Biodegradation by Cancer Cells of Magnetite Nanoflowers with and without Encapsulation in PS-b-PAA Block Copolymer Micelles. *ACS Appl. Mater. Interfaces* **2024**, *16* (27), 34772–34782. https://doi.org/10.1021/acsami.4c08727.
(24) Gao, W.; Sun, Y.; Cai, M.; Zhao, Y.; Cao, W.; Liu, Z.; Cui, G.; Tang, B. Copper Sulfide Nanoparticles as a Photothermal Switch for TRPV1 Signaling to Attenuate Atherosclerosis. *Nature Communications* **2018**, *9* (1), 231. https://doi.org/10.1038/s41467-017-02657-z.
(25) Russell, P.; Hagemeyer, C. E.; Esser, L.; Voelcker, N. H. Theranostic Nanoparticles for the Management of Thrombosis. *Theranostics* **2022**, *12* (6), 2773–2800. https://doi.org/10.7150/thno.70001.
(26) Patil, U. S.; Adireddy, S.; Jaiswal, A.; Mandava, S.; Lee, B. R.; Chrisey, D. B. In Vitro/In Vivo Toxicity Evaluation and Quantification of Iron Oxide Nanoparticles. *Int J Mol Sci* **2015**, *16* (10), 24417–24450. https://doi.org/10.3390/ijms161024417.
(27) Morais, P. C.; Silva, D. C. Mathematical Modeling for an MTT Assay in Fluorine-Containing Graphene Quantum Dots. *Nanomaterials* **2022**, *12* (3), 413. https://doi.org/10.3390/nano12030413.
(28) Arami, H.; Khandhar, A.; Liggitt, D.; Krishnan, K. M. In Vivo Delivery, Pharmacokinetics, Biodistribution and Toxicity of Iron Oxide Nanoparticles. *Chem Soc Rev* **2015**, *44* (23), 8576–8607. https://doi.org/10.1039/c5cs00541h.
(29) Pucci, C.; Degl'Innocenti, A.; Gümüş, M. B.; Ciofani, G. Superparamagnetic Iron Oxide Nanoparticles for Magnetic Hyperthermia: Recent Advancements, Molecular Effects, and Future Directions in the Omics Era. *Biomaterials Science* **2022**, *10* (9), 2103–2121. https://doi.org/10.1039/D1BM01963E.
(30) Agarwal, V.; Gupta, V.; Bhardwaj, V. K.; Singh, K.; Khullar, P.; Bakshi, M. S. Hemolytic Response of Iron Oxide Magnetic Nanoparticles at the Interface and in Bulk: Extraction of Blood Cells by Magnetic Nanoparticles. *ACS Appl. Mater. Interfaces* **2022**, *14* (5), 6428–6441. https://doi.org/10.1021/acsami.1c23496.
(31) Kaushik, S.; Thomas, J.; Panwar, V.; Ali, H.; Chopra, V.; Sharma, A.; Tomar, R.; Ghosh, D. In Situ Biosynthesized Superparamagnetic Iron Oxide Nanoparticles (SPIONS) Induce

Efficient Hyperthermia in Cancer Cells. *ACS Appl. Bio Mater.* **2020**, *3* (2), 779–788. https://doi.org/10.1021/acsabm.9b00720.
(32) Cabrera, D.; Eizadi Sharifabad, M.; Ranjbar, J. A.; Telling, N. D.; Harper, A. G. S. Clot-targeted Magnetic Hyperthermia Permeabilizes Blood Clots to Make Them More Susceptible to Thrombolysis. *Journal of Thrombosis and Haemostasis* **2022**, *20* (11), 2556–2570. https://doi.org/10.1111/jth.15846.
(33) Jia, J.-M.; Chowdary, P. D.; Gao, X.; Ci, B.; Li, W.; Mulgaonkar, A.; Plautz, E. J.; Hassan, G.; Kumar, A.; Stowe, A. M.; Yang, S.-H.; Zhou, W.; Sun, X.; Cui, B.; Ge, W.-P. Control of Cerebral Ischemia with Magnetic Nanoparticles. *Nature Methods* **2017**, *14* (2), 160–166. https://doi.org/10.1038/nmeth.4105.
(34) Fauconnier, N.; Bée, A.; Roger, J.; Pons, J. N. Synthesis of Aqueous Magnetic Liquids by Surface Complexation of Maghemite Nanoparticles. *Journal of Molecular Liquids* **1999**, *83* (1), 233–242. https://doi.org/10.1016/S0167-7322(99)00088-4.
(35) Söderström, A. C.; Nybo, M.; Nielsen, C.; Vinholt, P. J. The Effect of Centrifugation Speed and Time on Pre-Analytical Platelet Activation. *Clinical Chemistry and Laboratory Medicine (CCLM)* **2016**, *54* (12), 1913–1920. https://doi.org/10.1515/cclm-2016-0079.
(36) Rico, L. G.; Salvia, R.; Ward, M. D.; Bradford, J. A.; Petriz, J. Flow-Cytometry-Based Protocols for Human Blood/Marrow Immunophenotyping with Minimal Sample Perturbation. *STAR Protoc* **2021**, *2* (4), 100883. https://doi.org/10.1016/j.xpro.2021.100883.
(37) Vidmar, J.; Serša, I.; Kralj, E.; Tratar, G.; Blinc, A. Discrimination between Red Blood Cell and Platelet Components of Blood Clots by MR Microscopy. *Eur Biophys J* **2008**, *37* (7), 1235–1240. https://doi.org/10.1007/s00249-008-0336-6.
(38) Anoardo, E.; Galli, G.; Ferrante, G. Fast-Field-Cycling NMR: Applications and Instrumentation. *Appl. Magn. Reson.* **2001**, *20* (3), 365–404. https://doi.org/10.1007/BF03162287.
(39) Andreas, K.; Georgieva, R.; Ladwig, M.; Mueller, S.; Notter, M.; Sittinger, M.; Ringe, J. Highly Efficient Magnetic Stem Cell Labeling with Citrate-Coated Superparamagnetic Iron Oxide Nanoparticles for MRI Tracking. *Biomaterials* **2012**, *33* (18), 4515–4525. https://doi.org/10.1016/j.biomaterials.2012.02.064.
(40) Swanepoel, A. C.; Pretorius, E. Ultrastructural Analysis of Platelets during Three Phases of Pregnancy: A Qualitative and Quantitative Investigation. *Hematology* **2015**, *20* (1), 39–47. https://doi.org/10.1179/1607845413Y.0000000150.
(41) Herzenberg, L. A.; Tung, J.; Moore, W. A.; Herzenberg, L. A.; Parks, D. R. Interpreting Flow Cytometry Data: A Guide for the Perplexed. *Nat Immunol* **2006**, *7* (7), 681–685. https://doi.org/10.1038/ni0706-681.
(42) Rosmini, S.; Bulluck, H.; Abdel, -Gadir Amna; Treibel, T. A.; Culotta, V.; Thompson, R.; Piechnik, S. K.; Kellman, P.; Manisty, C.; Moon, J. C. The Effect of Blood Composition on T1 Mapping. *JACC: Cardiovascular Imaging* **2019**, *12* (9), 1888–1890. https://doi.org/10.1016/j.jcmg.2019.03.018.
(43) Fanost, A.; Jaber, M.; de Viguerie, L.; Korb, J.-P.; Levitz, P. E.; Michot, L. J.; Mériguet, G.; Rollet, A.-L. Green Earth Pigments Dispersions: Water Dynamics at the Interfaces. *Journal of Colloid and Interface Science* **2021**, *581*, 644–655. https://doi.org/10.1016/j.jcis.2020.07.085.
(44) Barberon, F.; Korb, J.-P.; Petit, D.; Morin, V.; Bermejo, E. Probing the Surface Area of a Cement-Based Material by Nuclear Magnetic Relaxation Dispersion. *Phys. Rev. Lett.* **2003**, *90* (11), 116103. https://doi.org/10.1103/PhysRevLett.90.116103.
(45) Korb, J.-P. Multiscale Nuclear Magnetic Relaxation Dispersion of Complex Liquids in Bulk and Confinement. *Progress in Nuclear Magnetic Resonance Spectroscopy* **2018**, *104*, 12–55. https://doi.org/10.1016/j.pnmrs.2017.11.001.

(46) Prakhya, K. S.; Vekaria, H.; Coenen, D. M.; Omali, L.; Lykins, J.; Joshi, S.; Alfar, H. R.; Wang, Q. J.; Sullivan, P.; Whiteheart, S. W. Platelet Glycogenolysis Is Important for Energy Production and Function. *Platelets* **2023**, *34* (1), 2222184. https://doi.org/10.1080/09537104.2023.2222184.
(47) Blair, P.; Flaumenhaft, R. Platelet α–Granules: Basic Biology and Clinical Correlates. *Blood Rev* **2009**, *23* (4), 177–189. https://doi.org/10.1016/j.blre.2009.04.001.
(48) Whiteheart, S. W. Fueling Platelets: Where Does the Glucose Come From? *Arterioscler Thromb Vasc Biol* **2017**, *37* (9), 1592–1594. https://doi.org/10.1161/ATVBAHA.117.309841.
(49) De Paoli, S. H.; Tegegn, T. Z.; Elhelu, O. K.; Strader, M. B.; Patel, M.; Diduch, L. L.; Tarandovskiy, I. D.; Wu, Y.; Zheng, J.; Ovanesov, M. V.; Alayash, A.; Simak, J. Dissecting the Biochemical Architecture and Morphological Release Pathways of the Human Platelet Extracellular Vesiculome. *Cell. Mol. Life Sci.* **2018**, *75* (20), 3781–3801. https://doi.org/10.1007/s00018-018-2771-6.
(50) Lacava, L. M.; Lacava, Z. G. M.; Da Silva, M. F.; Silva, O.; Chaves, S. B.; Azevedo, R. B.; Pelegrini, F.; Gansau, C.; Buske, N.; Sabolovic, D.; Morais, P. C. Magnetic Resonance of a Dextran-Coated Magnetic Fluid Intravenously Administered in Mice. *Biophysical Journal* **2001**, *80* (5), 2483–2486. https://doi.org/10.1016/S0006-3495(01)76217-0.
(51) Sobot, D.; Mura, S.; Couvreur, P. Nanoparticles: Blood Components Interactions. In *Encyclopedia of Polymeric Nanomaterials*; Kobayashi, S., Müllen, K., Eds.; Springer: Berlin, Heidelberg, 2021; pp 1–10. https://doi.org/10.1007/978-3-642-36199-9_227-1.

Table of contents